Highlighting the Reversible Manganese Electroactivity in Na-Rich Manganese Hexacyanoferrate Material for Li- and Na-Ion Storage

Angelo Mullaliu, Jakob Asenbauer, Giuliana Aquilanti, Stefano Passerini,* and Marco Giorgetti*

The electroactivity of sodium-rich manganese hexacyanoferrate (MnHCF) material constituted of only abundant elements, as insertion host for Li- and Na-ions is herein comprehensively discussed. This material features high specific capacities (>130 mAh g^{-1}) at high potentials when compared to other materials of the same class, i.e., Prussian blue analogs. The reversible electronic and structural modifications occurring during ion release/uptake, which are responsible for such high specific capacity, are revealed herein. The in-depth electronic and structural analysis carried out combining X-ray diffraction and X-ray absorption spectroscopy (XAS), demonstrates that both Fe and Mn sites are involved in the electrochemical process, being the high delivered capacity the result of a reversible evolution in oxidation states of the metallic centers (Fe^{3+}/Fe^{2+} and Mn^{2+}/Mn^{3+}). Along with the Mn^{2+}/Mn^{3+} oxidation, the Mn local environment experiences a substantial yet reversible Jahn–Teller effect, being the equatorial Mn-N distances shrunk by 10% (2.18 Å → 1.96 Å). Na-rich MnHCF material offers slightly higher performance upon uptake and release of Na-ions (469 Wh kg^{-1}) than Li-ions (457 Wh kg^{-1}), being, however, the electronic and structural transformation independent of the adopted medium, as observed by XAS spectroscopy.

Dr. A. Mullaliu, J. Asenbauer, Prof. S. Passerini
Helmholtz Institute Ulm (HIU)
Helmholtzstrasse 11, 89081 Ulm, Germany
E-mail: stefano.passerini@kit.edu
Dr. A. Mullaliu, J. Asenbauer, Prof. S. Passerini
Karlsruhe Institute of Technology (KIT)
P.O. Box 3640, 76021 Karlsruhe, Germany
Dr. G. Aquilanti
Elettra Sincrotrone Trieste
ss 14, km 163.5, Basovizza 34149, Trieste, Italy
Prof. M. Giorgetti
Department of Industrial Chemistry "Toso Montanari,"
University of Bologna
Viale Risorgimento 4, 40136 Bologna, Italy
E-mail: marco.giorgetti@unibo.it

1. Introduction

Affordable energy is a key factor for the sustainable economic growth.[1] Batteries play a crucial role due to their ability to reversibly store and release energy when needed.[2] Li-ion batteries will be the leading chemistry for electromobility in the next decade,[3] therefore new battery chemistries, employing abundant, safe, and environmentally friendly electrode materials, but avoiding graphite, Ni, and particularly Co,[4] are actively investigated. Manganese hexacyanoferrates (MnHCFs), composed of only abundant metals, display large reversible specific capacities (>120 mAh g^{-1}) and high potentials for the storage of Li,[5] Na,[6] and K[7] in aprotic electrolytes compared to other Prussian blue analogs (PBAs).[8] Although the electrochemical activity of MnHCF has been proposed in several works,[5,9–14] clear evidences of its origin and evolution upon the alkali metal uptake and release are still missing. This information, however, is particularly relevant because of the Jahn–Teller (JT) effect affecting all trivalent Mn-based materials. Here, we report the X-ray absorption spectroscopy (XAS) investigation of Na-rich MnHCF upon full removal and insertion of Li$^+$ and Na$^+$ ions. Due to the involved physical phenomena and the penetrating character of synchrotron hard X-rays, electronic and spin configurations, and local structural environment around the transition metals (photo absorber) can be investigated, providing clear insight into the bulk modifications arising from electrochemical processes. The in-depth analysis of the XANES (X-ray absorption near-edge structure) and EXAFS (extended X-ray absorption fine structure) signals shows the Fe^{2+}/Fe^{3+} and Mn^{2+}/Mn^{3+} redox processes, however, accompanied with strong structural modifications at the Mn site. Nonetheless, in spite of the large JT related deformation of the Mn environment, the material shows a full electrochemical, electronic, and structural reversibility. Finally, the Na-rich MnHCF material offers slightly higher performance in metal anode cells upon uptake and release of Na-ions (469 Wh kg^{-1}) than Li-ions (457 Wh kg^{-1}).

**ADVANCED
SCIENCE NEWS**
www.advancedsciencenews.com
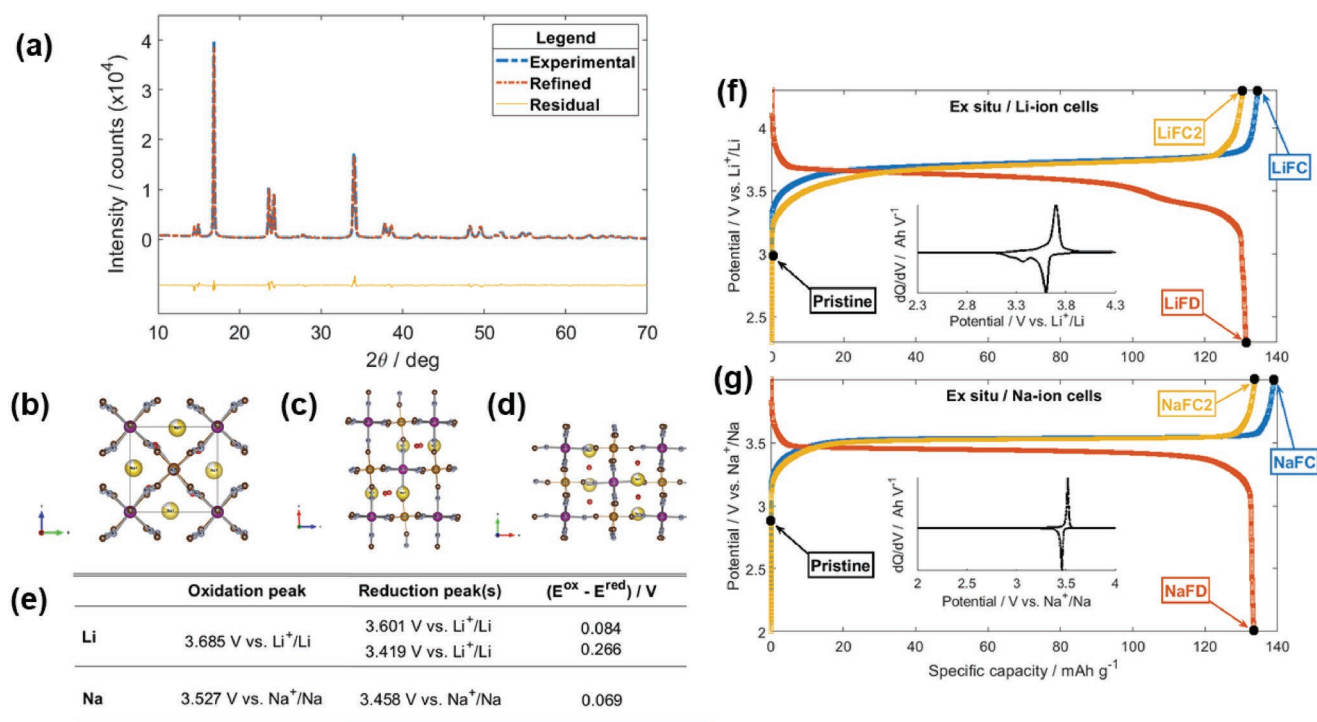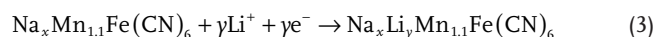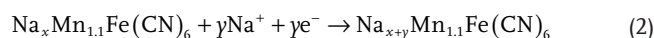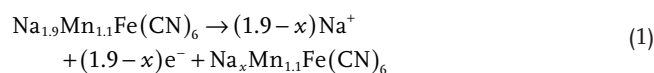
**small
methods**
www.small-methods.com

Figure 1. Structural and electrochemical characterization. a) XRD pattern and Rietveld refinement on Na-rich MnHCF powder. Lattice views along the b) *a*, c) *b*, and d) *c* axes. e) Redox potential values for the Li-ion and Na-ion insertion and removal as detected in the first cycle of panels (f) and (g). Potential profiles upon electrochemical removal (charge, C) and insertion (discharge, D) of f) Li- and g) Na-ions in the Na-rich MnHCF electrodes. The corresponding differential capacity plots are illustrated in the insets. The LiFC, LiFD, LiFC2, NaFC, NaFD, and NaFC2 markers define the state of charge of the electrodes used for the ex situ XAS investigation (see the Experimental Section).

2. Results and Discussion

The X-ray diffraction (XRD) pattern of the in-house synthesized and vacuum-dried Na-rich MnHCF is reported in **Figure 1**a together with the Rietveld refinement. This latter was carried out assuming the material's formula to be $Na_{1.9}Mn_{1.1}Fe(CN)_6$ (see the Supporting Information). The overall quality of the fit is good with lattice parameters and atomic positions well agreeing with the reported values (see Table S2, Supporting Information), thus confirming the material structural model presented in Figure 1b.[15] Unlike most PBAs, MnHCF features a monoclinic lattice (space group $P2_1/n$, unique *b*-axis), with *a*, *b*, *c*, and β assuming values equal to 10.562(5), 7.534(4), 7.356(4) Å, and 92.01(4)°, respectively (see Table S2, Supporting Information). Both Fe and Mn atoms are located in octahedral environments, the Fe sites (2d Wyckoff position) being surrounded by C-atoms, while the Mn sites (2a) coordinated to N-atoms, with the C- and N-ends defining cyanide bridges. Water molecules and interstitial sodium (NA) ions are placed in 4e sites.

Following the extensive vacuum dehydration, the Na-rich MnHCF electrodes were assembled into Li- and Na-cells as described in the Experimental Section. The potential profiles upon the electrochemical alkali ion removal (C) and insertion (D), respectively, from and in Na-rich MnHCF are depicted in Figure 1f,g, while reaction processes taking place during charge and discharge are presented in Equations (1)–(3). The potential profiles differ from the Li- to Na- cells, with a higher slope for the former due to a multiple step insertion mechanism (see

Figure 1e). During the positive polarization, the desodiation of the material (see Equation (1)) takes place in a single extraction process within a narrow potential window. While the following sodiation (see Equation (2)) occurs in a single step (Figure 1g), the lithium insertion process (Figure 1f and Equation (3)) takes place at two different potential values (see Figure 1e). In the second alkali ion removal step, however, a single voltage plateau is observed for both Li- and Na-ions

$$Na_{1.9}Mn_{1.1}Fe(CN)_6 \rightarrow (1.9-x)Na^+ \\ +(1.9-x)e^- + Na_xMn_{1.1}Fe(CN)_6 \tag{1}$$

$$Na_xMn_{1.1}Fe(CN)_6 + \gamma Na^+ + \gamma e^- \rightarrow Na_{x+\gamma}Mn_{1.1}Fe(CN)_6 \tag{2}$$

$$Na_xMn_{1.1}Fe(CN)_6 + \gamma Li^+ + \gamma e^- \rightarrow Na_xLi_\gamma Mn_{1.1}Fe(CN)_6 \tag{3}$$

where $0.10 \leq x \leq 0.15$ and $1.65 \leq \gamma \leq 1.70$ according to the electrochemical curves.

While the voltage signature of the Na-rich MnHCF material upon Na-ion removal and insertion well agrees with literature data,[15] that involving Li-ions differs.[5,16] In more details, the corresponding differential capacity plots corresponding to the Li-ion removal and uptake (see inset in Figure 1f) present a well-defined reduction peak above 3.6 V, but only a hint for the cathodic peak at about 3.4 V is visible. This could be due to the higher degree of dehydration of the Na-rich MnHCF material
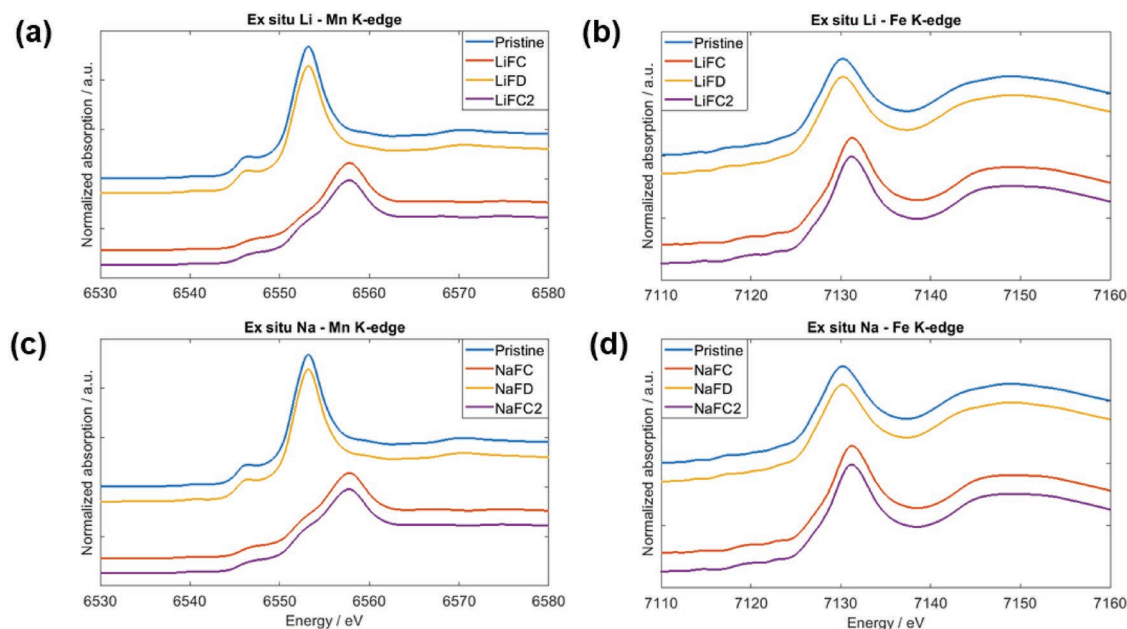
Figure 2. Ex situ XANES spectra of Na-rich MnHCF electrodes. Recorded XANES spectra for electrodes extracted from a,b) Li- and c,d) Na-cells at both a,c) Mn K-edge and b,d) Fe K-edge.

herein employed with respect to the reported literature.[5,9] Moreover, the main redox process occurs at higher potential in the Na-cell since its potential is shifted to less than 0.2 V compared to the Li-cell while the Na^+/Na couple is ≈300 mV higher than the Li^+/Li couple. Energy densities related to the discharge process for Li- and Na-cells are comparable, being 457 and 469 Wh kg^{-1}, respectively. Additionally, Na-cells present a flatter profile than respective Li-cells, being 97% of the displayed reversible capacity (referred to discharge) supplied within a narrow potential window (equal to 0.46 V).

The electrochemical performance of an electrode material derives from a combination of structural and electronic properties and their reversible evolution upon the charge and discharge processes. XAS, providing insight into the transition metal centers, is a powerful technique to investigate the Na-rich MnHCF electrodes. Synchrotron-based X-rays are generated by trajectory deflection of relativistic electrons in circular evacuated pipes and offer a multitude of experimental advantages, such as high intensity and brilliance, and a broad and continuous spectrum. The incident beam can be tuned to match the energy required to the 1s core electron ejection in transition metals (K-edge absorption), whose value is an unambiguous fingerprint of the selected metal. Due to the involved physical phenomena and the penetrating character of hard X-rays, electronic and spin configurations, and local structural environment around the photo absorber can be investigated in energy materials, providing clear insight into the bulk modifications arising from electrochemical processes.

Ex situ XANES spectra were recorded at the Mn (**Figure 2**a,c) and Fe K-edge (Figure 2b,d) of Na-rich MnHCF electrodes extracted from both the Li- (panel a,b) and Na-cells (panel c,d) at fully oxidized, reduced, and successively re-oxidized states (see Figure 1f,g and **Table 1** for samples labels). The Mn K-edge evolution in both media suggests a deep modification of the Mn

local environment, as well its strong oxidation as a result of the alkali ion removal, being the energy of the white line shifted roughly 5 eV toward higher energy. The Fe K-edge displays a similar trend with a small, yet significant energy shift of 1 eV. Concerning both metal edges, the overlap between the spectra of pristine and discharged samples, as well spectra of fully charged ones, is indicative of a highly reversible character of the material during cycling. The evolution of such features appears to be independent of the alkali ion, highlighting not only the Mn electroactivity in Na-rich MnHCF, but also its reversible character.

The Mn^{2+}/Mn^{3+} oxidation has both electronic and structural effects, being Mn^{3+} JT active. The removal of one electron in the e_g orbital from high spin (HS) Mn^{2+} (d^5 configuration)[17] causes a basal plane shrinkage (see **Figure 3**e), as further corroborated by EXAFS analysis, as well as a different orbital distribution, being the d_z^2 way less perturbed than the $d_{x^2-y^2}$ by the potential generated by the cyanides.[18]

Concerning the transitions that occur from the 1s core level to the 3d/4p orbitals in the pre-edge region of the K-edge

Table 1. Cycling conditions for all ex situ electrodes.

| Sample name	Cycling conditions
Pristine	Pristine electrode (pressed and vacuum dried)
LiFC	Fully oxidized to 4.3 V versus Li^+/Li at 0.1 C
LiFD	Fully reduced to 2.3 V versus Li^+/Li at 0.1 C after first charge to 4.3 versus Li^+/Li at 0.1 C
LiFC2	Fully oxidized to 4.3 V versus Li^+/Li at 0.1 C after one full cycle
NaFC	Fully oxidized to 4.0 V versus Na^+/Na at 0.1 C
NaFD	Fully reduced to 2.0 V versus Na^+/Na at 0.1 C after first charge to 4.0 versus Li^+/Li at 0.1 C
NaFC2	Fully oxidized to 4.0 V versus Na^+/Na at 0.1 C after one full cycle
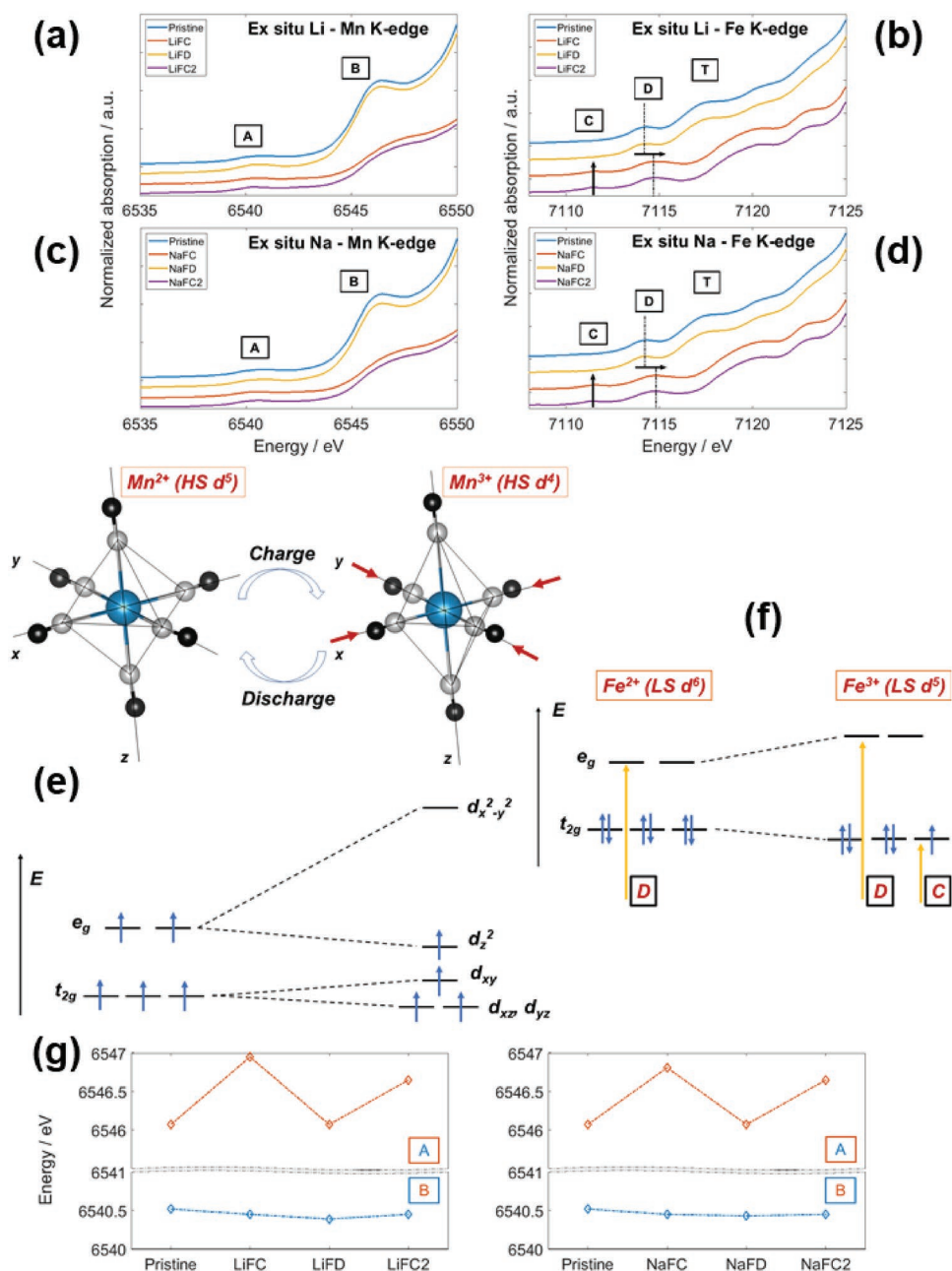
Figure 3. Pre-peak analysis of the K-edge region. Pre-edge evolution for ex situ samples: a) Mn- and b) Fe-edge of ex situ Li samples; c) Mn- and d) Fe-edge of ex situ Na samples. e) Schematic diagram of Mn 3d orbitals after JT-elongation; f) Schematic diagram of Fe 3d orbitals. g) Evolution of peaks A and B for all states of charge.

XAS spectra (see Figure 3a,b), those that are considered to be taken place in the t_{2g}/e_g[19] and 4p orbitals in Mn^{2+} species are labeled as A and B, respectively. In the case of JT-active Mn^{3+} (d^4 configuration), the structural distortion derives from a loss of symmetry around the Mn site, i.e., a decrease in energy degeneration for 3d orbitals. By considering principally two main transitions' events, i.e., A and B, well-separated in energy, a clear broadening is observed for peak B in Figure 3g and Figure S4 in the Supporting Information for all charged states. This can be related to the single transition to an unoccupied 4p orbital, but also to a high energy transition to the

$d_{x^2-y^2}$ orbital after JT-elongation (whose energy value matches with the predicted one in ref. [18] in case of an HS d^4 configuration). The broad peak shape featured by peak B only for fully charged samples, as displayed in Figure S4 in the Supporting Information, is consistent with a multi-transition contribution occurring only in the JT-distorted Mn^{3+}. The obtained pattern in Figure 3g is a reflection of the high reversibility along cycling and the apparent equivalence between Li and Na media. On the other side, the JT effect does not affect much the A transition, likely because the energy center of gravity of the newly distributed orbitals is similar to the original value of the 3d orbitals.
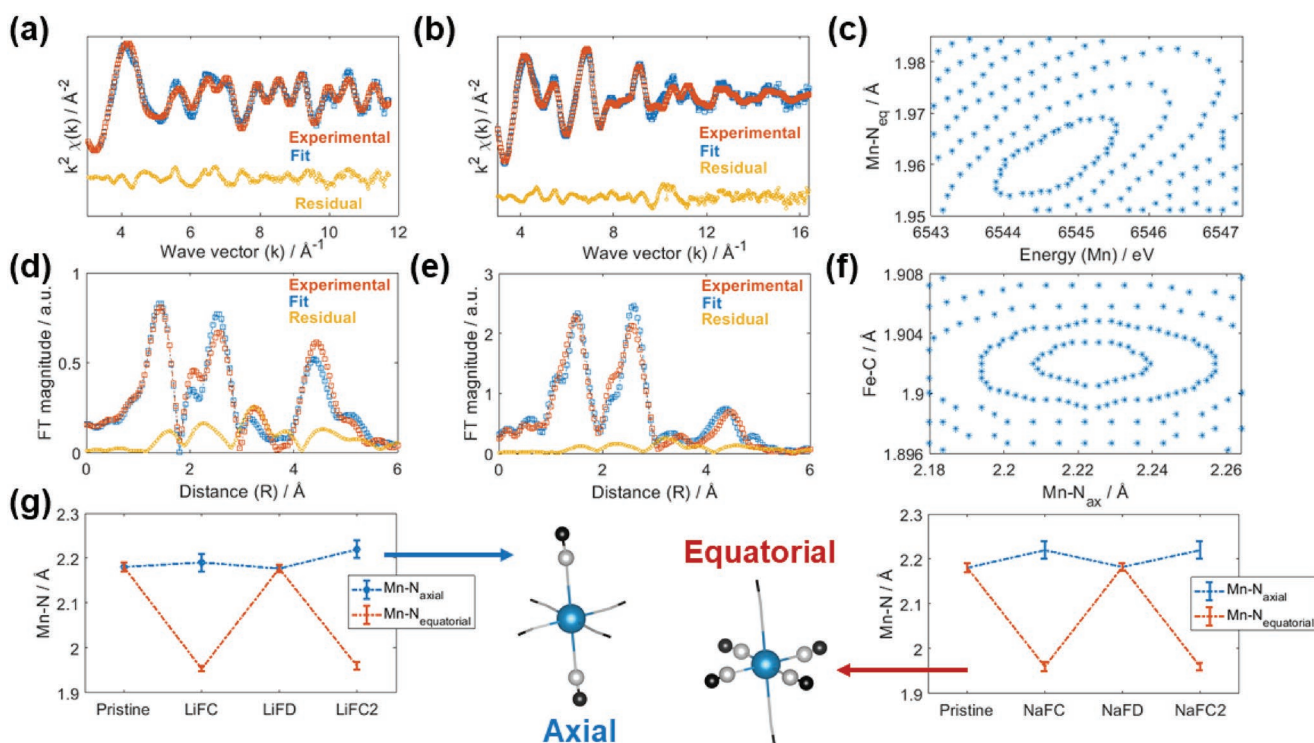
**ADVANCED
SCIENCE NEWS**
www.advancedsciencenews.com

**small
methods**
www.small-methods.com

Figure 4. Main results of the EXAFS analysis. a,b,d,e) EXAFS fitting analysis for LiFC. Comparison between experimental and theoretical EXAFS signal at the a) Mn and b) Fe K-edges, and d,e) corresponding Fourier transform signals. c,f) Contour plots for the error parameter determination. g) Evolution of axial and equatorial Mn-N distances with state of charge for both Li- and Na-cells.

Besides, the Fe pre-edge region is appreciably modified as a consequence of the different electronic occupancy in the t_{2g} orbitals, as presented in Figure 3f. By taking a closer look at the dipole forbidden but quadrupole allowed 1s-3d transitions,[20] pristine and fully discharged sample features a single transition around 7114 eV (labeled as D, see Figure 3b), while fully charged samples display two transitions, respectively at 7111 eV (labeled as C, see Figure 3b) and 7114 eV (peak D). As schematically shown in Figure 3f, Fe^{II} sixfolded coordinated to the C-end of cyanide ligands is expected to be found in its low-spin state (LS-Fe^{II}) with a $t_{2g}^6 e_g^0$ electron configuration and spin multiplicity $S = 0$. Hence, only one possible transition is expected to the 3d-e_g orbitals (peak D ≈7114 eV). On the other hand, low spin Fe^{III} (LS-Fe^{III}) has a $t_{2g}^5 e_g^0$ electron configuration and spin multiplicity $S = 2$. Two possible transitions are expected, i.e., 1s-3dt_{2g} (peak C ≈7111 eV) and 1s-3 de_g (peak D ≈7114 eV), suggesting a ΔO_h ~ 2.8 eV, in line with the values for other molecular bimetallic complexes of the same family.[21] Fe^{III} e_g orbitals have slightly higher energy than respective Fe^{II} orbitals (Δ ~ 0.4 eV), explaining the shift of the 1s-3d e_g transition after cycling. Transitions occurring at higher energies (>7115 eV, generically labeled as T, see Figure 3b) below the threshold arise from normally forbidden dipole transitions to empty bound states that reflect longer-range effects of the shells beyond the cyanides,[22–24] and their rise in energy is consistent with the shift of such states to higher energies upon oxidation.

Overall, the ex situ XANES investigation reveals the electroactive capability of both metal sites, i.e., both Fe and Mn are contributing to the charge compensation during charge and discharge, and that Na-rich MnHCF undergoes the same modifications upon Li or Na storage and release, since the resulting XANES curves display identical trends.

The JT-effect implies strong structural effects at the Mn site. **Figure 4** presents the details of the EXAFS analysis. Although only few multiple scattering (MS) signals were necessary to fit the experimental signals (see Supporting Information), the fit quality reported in panels (a), (b), (d), and (e) is good. The Mn environment consists of MnN_6 octahedra, symmetric in the pristine state with the Mn-N distance being 2.18 Å. Asymmetric Mn-N shells were preliminarily considered for all states of charge (see Table S4, Supporting Information), however, the analysis results suggest a symmetric Mn site in the reduced states. To minimize the number of refinable parameters, two structural models were considered for reduced and oxidized states, adopting a symmetric Mn-N shell for the former and an asymmetric Mn site environment for the latter. The four Mn-N equatorial distances contract to ≈1.96 Å (about 10%) in oxidized states, being completely restored after reduction, while axial Mn-N distances remain roughly constant (Figure 4g). Therefore, the JT-effect is quantified as basal shrinkage rather than axial elongation, and it is seen to be the same, within the experimental errors given by the contour plots (Figure 4c,f), for both Li and Na half-cells.

3. Conclusion

Our results show the high specific capacity and energy density displayed by Na-rich MnHCF derived from the electroactivity

1900529 (5 of 7)

**ADVANCED
SCIENCE NEWS**

www.advancedsciencenews.com

**small
methods**

www.small-methods.com

of both metals. The reported reversibility is both electronic and structural, evidenced by a reversible local rearrangement. While the Fe structural environment is not particularly affected by the electrochemical process, although an evolution in oxidation state ($Fe^{2+} \rightarrow Fe^{3+}$) is distinctly appreciated during charge, the Mn local environment experiences a reversible JT-effect along with the Mn^{2+}/Mn^{3+} oxidation. Identical trends in Li-ion and Na-ion cells are observed by XAS spectroscopy, being the electronic and structural transformation independent by the adopted medium. Unlike other Mn-active compounds, such as lithium metal oxides, where the JT-active Mn^{3+} undergoes a disproportionation into Mn^{2+} and Mn^{4+},[25] which decreases irreversibly the initial specific capacity, the cyanide first-shell environment around the Mn site seems to hinder the capacity fade and to promote a reversible Mn^{2+}/Mn^{3+} redox.

4. Experimental Section

Synthesis: Na-rich MnHCF was synthesized through a simple and scalable co-precipitation method involving the reaction of manganese sulfate monohydrate ($MnSO_4 \cdot H_2O$) and sodium ferrocyanide decahydrate ($Na_4[Fe(CN)_6] \cdot 10H_2O$), which were used as received (Sigma Aldrich) without further purification. Concisely, the solutions of the two reagents (0.1 L, 0.1000 M each) were simultaneously dropwise poured to an aqueous solution (0.1 M, 0.1000 M) of sodium sulfate Na_2SO_4 (Sigma Aldrich) by means of a peristaltic pump at a rate of 3.8 mL min^{-1}. Both reagents and reaction batch were kept at constant temperature (40 ± 2 °C) using a thermostated bath. The experimental setup is reported in the Supporting Information. Magnetic stirring was adopted throughout the addition, which was stopped 2 min after the complete addition of the reagents. The obtained suspension containing Na-rich MnHCF had a pale brown color. The solution was aged for 5 days, assuring complete decantation, then the precipitate was collected via centrifugation at 3500 rpm for 30 min using test tubes containing about 5 mL of suspension. After removing the supernatant, the precipitate was washed three times with ≈2 mL of distilled water per test tube, then grounded in an agate mortar and dried at 60 °C for 48 h.

Characterization: Thermogravimetric analysis (TGA) was carried out (TA Discovery TGA instrument) started at 40 °C after an equilibration time of 30 min, and heated to 500 °C with a ramp of 5 °C min^{-1} in a N_2 atmosphere.

Inductively coupled plasma–optical emission spectrometry was carried out by means of a Spectro Arcos FHS12 instrument. About 10 mg of samples was dissolved in the nitric acid/hydrochloric acid solution (3/1 volumetric ratio) by heating to 200 °C in a MARS 6 iWave microwave oven. Afterward, the dissolved samples were diluted with water to achieve clear solutions, which were thermally equilibrated at 20 °C. At least two individual solutions were prepared to check reproducibility of results.

The XRD spectrum of the Na-rich MnHCF was recorded on the pristine powder by means of a Bruker D8 Advance diffractometer equipped with a Cu Kα source (λ = 0.15406 nm) in the 10° < 2θ < 70° range with a step size of 0.029745° and an acquisition time of 2 s point^{-1}. Rietveld refinement was performed using FullProf Suite software[26] and assuming as a structural model the one reported by Song et al.[15] A Thompson–Cox–Hastings pseudo-Voigt peak shape was used. Factor scale, peak shape parameters, cell parameters, background, and atomic parameters were refined in this order. Graphical representation of structures was exploited by means of VESTA software.[27]

Electrodes Preparation and Electrochemical Characterization: The cathode slurry was prepared by mixing 85 wt% of active material (Na-rich MnHCF), 10 wt% conductive agent (Super C65, IMERYS), and 5 wt% binder (polyvinylidene difluoride; Solef 6020, Solvay Polymerspecialties). This latter component was previously dissolved (10 wt% solution) in dried *N*-methyl-2-pyrrolidone, (NMP). Additional NMP was added to adjust the viscosity of the slurry. The final solid

content $\left(\dfrac{m(\text{solid})}{m(\text{solid} + \text{solvent})} \right)$ was 0.20. The materials were mixed using a ball milling procedure consisting of two repetitions of 1 h each with a 10 min break in between stages. The slurries were cast on aluminum foil (thickness 20 μm, previously cleaned with ethanol and dried at 80 °C overnight) using a blade coater (blade height of 200 μm), and successively dried at 60 °C overnight. Disk electrodes with a diameter of 12 mm were cut using a Hohsen puncher. The electrodes containing the Na-rich MnHCF material were weighed and pressed at 10 tons for 10 s. The final electrodes were extensively dried at 120 °C under vacuum (10^{-6} bar) for 24 h and finally stored in an Ar-filled glove box. The areal loading of the electrodes had a Student's *t*-distribution of 2.47 ± 0.04 mg_{MnHCF} cm^{-2} considering a population of 24 electrodes, and a confidence interval equal to 0.95. Electrode thickness was measured through a Mitutoyo C112XBS micrometer (precision 1 μm) after pressing and vacuum dehydrating. Electrode thickness values were in the 19 ± 2 μm range, after subtracting the thickness of Al collector, by considering a random population of seven electrodes and a confidence interval equal to 0.95.

Cell assembly was occurred in Ar-filled glove boxes (MBRAUN MB 200B ECO) with oxygen and water contents lower than 0.1 ppm, specifically dedicated to either only lithium or sodium battery assembly. Formulated Na-rich MnHCF material was adopted as the positive electrode in three-electrode Swagelok cells, using as counter (negative) and reference electrodes either Li metal or Na metal. GF/A Whatman paper was used as separator to avoid direct electrical contact between the positive, negative, and reference electrodes. LP30, i.e., 1.0 M $LiPF_6$ dissolved in the 1:1 volumetric mixture of ethylene carbonate and dimethyl carbonate (EC/DMC = 50/50 v/v) or 1 M $NaPF_6$ in propylene carbonate (PC) were employed as electrolytes for Li- and Na-cells, respectively. Galvanostatic cycling with potential limitation in constant current mode was performed on a battery cycler (Maccor, Series 4000). The nominal capacity of 152 mAh g^{-1} (1 C = 152 mAh g^{-1}) was considered for the weighed electrodes (i.e., containing interstitial water). Cycling was performed in the 2.3 < *E* < 4.3 V versus Li$^+$/Li or in the 2.0 < *E* < 4.0 V versus Na$^+$/Na starting at open circuit potential with a positive initial polarization. All tests were performed in climatic chambers at a temperature of 20 ± 2 °C.

Samples for ex situ XAS were obtained for both Li and Na cells (details are given in Table 1). To prevent any moisture contamination, the cells were disassembled after cycling in Ar-filled gloveboxes, electrodes were removed and rinsed with DMC (Li-ion cells) or PC (Na-ion cells), sandwiched between two polypropylene sheets and sealed under vacuum.

Ex situ XAS: XAS experiments were performed at Elettra–Sincrotrone Trieste (Italy), at the XAFS beamlines.[28] The storage ring was operated at 2.0 GeV in top-up mode with a typical current of 310 mA. XAS data were recorded at Mn and Fe K-edges in transmission mode using ionization chambers filled with a mixture of Ar, N_2, and He to have 10%, 70%, and 95% of absorption in the I_0, I_1, and I_2 chambers. Internal reference, manganese and iron foils were used for energy calibration in each scan, allowing the continuous monitoring of the energy during consecutive scans. No energy drifts of the monochromator were observed during the experiments. Spectra at Mn and Fe K-edges were collected with a constant *k*-step of 0.03 Å^{-1} with 2 s point^{-1} acquisition time. Data were collected alternatingly from 6339 to 7110 eV and from 6912 to 8346 eV around the Mn and Fe K-edges, respectively. The energies were calibrated assigning the first inflection point of the metallic manganese and iron spectra to 6539 and 7112 eV, respectively. XAS data pre-treatment was carried out by means of ATHENA graphical utility.[29] The EXAFS analysis was performed using the GNXAS package[30,31] which was based on the MS theory. The method used the decomposition of the EXAFS signals into a sum of several contributions, namely, the n-body terms. The theoretical signal was calculated ab initio and contained the relevant two-body $\gamma^{(2)}$, three-body $\gamma^{(3)}$, and four-body $\gamma^{(4)}$ MS terms.[32] The two-body terms were associated with pairs of atoms and probed their distances and variances. The three-body terms were associated with triplets of atoms and probe angles, and bond–bond and bond–angle

**ADVANCED
SCIENCE NEWS**

www.advancedsciencenews.com

**small
methods**

www.small-methods.com

correlations. The four-body terms were associated with chains of four atoms, and probe distances and angles in-between, and bond–bond and bond–angle correlations. However, since Fe-C-N-Mn chains featured angles in-between close to 180°, the actual number of parameters used to define the $\gamma^{(3)}$ or the $\gamma^{(4)}$ peaks was reduced by symmetry. More details on the use of parameters correlation in the four-body term is out of the aim of the present work and can be found in refs. [33,34]. Data analysis was performed by minimizing a χ^2-like residual function that compared the theoretical (model) signal, $\mu m_{od}(E)$, to the experimental one, $\mu_{exp}(E)$. The phase shifts for the photoabsorber and backscatterer atoms were calculated starting from the structure reported by Song et al.[15] according to the muffin-tin approximation and allowing 10% overlap between the muffin-tin spheres. The Hedin–Lundqvist complex potential[35] was used for the exchange–correlation potential of the excited state. The core-hole lifetime, Γ_c, was fixed to the tabulated value[36] and was included in the phase shift calculation.

Supporting Information

Supporting Information is available from the Wiley Online Library or from the author.

Conflict of Interest

The authors declare no conflict of interest.

[1] S. Chu, A. Majumdar, *Nature* **2012**, *488*, 294.
[2] J. M. Tarascon, M. Armand, *Nature* **2001**, *414*, 359.
[3] D. Bresser, K. Hosoi, D. Howell, H. Li, H. Zeisel, K. Amine, S. Passerini, *J. Power Sources* **2018**, *382*, 176.
[4] C. Vaalma, D. Buchholz, M. Weil, S. Passerini, *Nat. Rev. Mater.* **2018**, *3*, 18013.
[5] Y. Kurihara, T. Matsuda, Y. Moritomo, *Jpn. J. Appl. Phys.* **2013**, *52*, 017301.
[6] T. Matsuda, M. Takachi, Y. Moritomo, *Chem. Commun.* **2013**, *49*, 2750.
[7] X. Bie, K. Kubota, T. Hosaka, K. Chihara, S. Komaba, *J. Mater. Chem. A* **2017**, *5*, 4325.
[8] J. Qian, C. Wu, Y. Cao, Z. Ma, Y. Huang, H. Ai, H. Yang, *Adv. Energy Mater.* **2018**, *8*, 1702619.
[9] M. Pasta, R. Y. Wang, R. Ruffo, R. Qiao, H. W. Lee, B. Shyam, M. Guo, Y. Wang, L. A. Wray, W. Yang, M. F. Toney, Y. Cui, *J. Mater. Chem. A* **2016**, *4*, 4211.
[10] K. Nakamoto, R. Sakamoto, M. Ito, A. Kitajou, S. Okada, *Electrochemistry* **2017**, *85*, 179.
[11] L. Wang, Y. Lu, J. Liu, M. Xu, J. Cheng, D. Zhang, J. B. Goodenough, *Angew. Chem., Int. Ed.* **2013**, *52*, 1964.
[12] Y. Moritomo, S. Urase, T. Shibata, *Electrochim. Acta* **2016**, *210*, 963.
[13] H. Wang, E. Xu, S. Yu, D. Li, J. Quan, L. Xu, L. Wang, Y. Jiang, *ACS Appl. Mater. Interfaces* **2018**, *10*, 34222.
[14] L. Jiang, Y. Lu, C. Zhao, L. Liu, J. Zhang, Q. Zhang, X. Shen, J. Zhao, X. Yu, H. Li, X. Huang, L. Chen, Y. S. Hu, *Nat. Energy* **2019**, *4*, 495.
[15] J. Song, L. Wang, Y. Lu, J. Liu, B. Guo, P. Xiao, J. J. Lee, X. Q. Yang, G. Henkelman, J. B. Goodenough, *J. Am. Chem. Soc.* **2015**, *137*, 2658.
[16] Y. Kurihara, Y. Moritomo, *Jpn. J. Appl. Phys.* **2014**, *53*, 067101.
[17] Y. Lu, L. Wang, J. Cheng, J. B. Goodenough, *Chem. Commun.* **2012**, *48*, 6544.
[18] J. Conradie, *Inorg. Chim. Acta* **2019**, *486*, 193.
[19] F. Farges, *Phys. Rev. B* **2005**, *71*, 155109.
[20] A. Mullaliu, G. Aquilanti, P. Conti, J. R. Plaisier, M. Fehse, L. Stievano, M. Giorgetti, *J. Phys. Chem. C* **2018**, *122*, 15868.
[21] M. Giorgetti, G. Aquilanti, M. Ciabocco, M. Berrettoni, *Phys. Chem. Chem. Phys.* **2015**, *17*, 22519.
[22] K. Hayakawa, K. Hatada, P. D'Angelo, S. Della Longa, C. R. Natoli, M. Benfatto, *J. Am. Chem. Soc.* **2004**, *126*, 15618.
[23] A. Bianconi, M. Dell'Ariccia, P. J. Durham, J. B. Pendry, *Phys. Rev. B* **1982**, *26*, 6502.
[24] N. Kosugi, T. Yokoyama, H. Kuroda, *Chem. Phys.* **1986**, *104*, 449.
[25] M. M. Thackeray, *Prog. Solid State Chem* **1997**, *25*, 1.
[26] J. Rodríguez-Carvajal, *Phys. B* **1993**, *192*, 55.
[27] K. Momma, F. Izumi, *J. Appl. Crystallogr.* **2011**, *44*, 1272.
[28] G. Aquilanti, M. Giorgetti, R. Dominko, L. Stievano, I. Arčon, N. Novello, L. Olivi, *J. Phys. D: Appl. Phys.* **2017**, *50*, 074001.
[29] B. Ravel, M. Newville, *J. Synchrotron Radiat.* **2005**, *12*, 537.
[30] A. Filipponi, A. Di Cicco, C. R. Natoli, *Phys. Rev. B* **1995**, *52*, 15122.
[31] A. Filipponi, A. Di Cicco, *Phys. Rev. B* **1995**, *52*, 15135.
[32] M. Giorgetti, M. Berrettoni, A. Filipponi, P. J. Kulesza, R. Marassi, *Chem. Phys. Lett.* **1997**, *275*, 108.
[33] M. Giorgetti, M. Berrettoni, *Inorg. Chem.* **2008**, *47*, 6001.
[34] M. Giorgetti, L. Guadagnini, D. Tonelli, M. Minicucci, G. Aquilanti, *Phys. Chem. Chem. Phys.* **2012**, *14*, 5527.
[35] L. Hedin, B. I. Lundqvist, S. Lundqvist, *Solid State Commun.* **1971**, *9*, 537.
[36] M. O. Krause, J. H. Oliver, *J. Phys. Chem. Ref. Data* **1979**, *8*, 329.

1900529 (7 of 7)